HHS Public Access

Author manuscript

Biomaterials. Author manuscript; available in PMC 2019 April 01.

Published in final edited form as:

Biomaterials. 2018 April ; 161: 203–215. doi:10.1016/j.biomaterials.2018.01.044.

Self-Indicating, Fully Active Pharmaceutical Ingredients Nanoparticles (FAPIN) for Multimodal Imaging Guided Trimodality Therapy

Xiangdong Xue[1,†], **Yee Huang**[1,3,†], **Xinshuai Wang**[1], **Zhongling Wang**[1], **Randy P. Carney**[1], **Xiaocen Li**[1], **Ye Yuan**[1], **Yixuan He**[1], **Tzu-yin Lin**[2], and **Yuanpei Li**[1,*]

[1]Department of Biochemistry and Molecular Medicine, UC Davis Comprehensive Cancer Center, University of California Davis, Sacramento, CA 95817, USA

[2]Division of Hematology/Oncology, Department of Internal Medicine, University of California Davis, Sacramento, California 95817, USA

[3]Institute of Aminal Husbandry and Veterinary Science, Zhejiang Academy of Agricultural Sciences, Hangzhou, Zhejiang 310021, China

Abstract

Conventional drug delivery systems contain substantial amounts of excipients such as polymers and lipids, typically with low drug loading capacity and lack of intrinsic traceability and multifunctionality. Here, we report fully active pharmaceutical ingredient nanoparticles (FAPIN) which were self-assembled by minimal materials, but seamlessly orchestrated versatile theranostic functionalities including: i) self-delivery: no additional carriers were required, all components in the formulation are active pharmaceutical ingredients; ii) self-indicating: no additional imaging tags were needed. The nanoparticle itself was composed of 100% imaging agents, so that the stability, drug release, subcellular dispositions, biodistribution and therapeutic efficacy of FAPINs can be readily visualized by ample imaging capacities, including energy transfer relay dominated, dual-color fluorogenic property, near-infrared fluorescence imaging and magnetic resonance imaging; and iii) highly effective trimodality cancer therapy, encompassing photodynamic-, photothermal- and chemo-therapies. FAPINs were fabricated with very simple material (a photosensitizer-drug conjugate), unusually achieved ~10 times better *in vitro* antitumor activity than their free counterparts, and were remarkably efficacious in patient-derived xenograft (PDX) glioblastoma multiforme animal models. Only two doses of FAPINs enabled complete ablation of highly-malignant PDX tumors in 50% of the mice.

TOC image

*Address correspondence to Yuanpei Li, lypli@ucdavis.edu.
†X. Xue and Y. Huang contributed equally to this work.

Competing interests

The authors declare no competing financial interest.

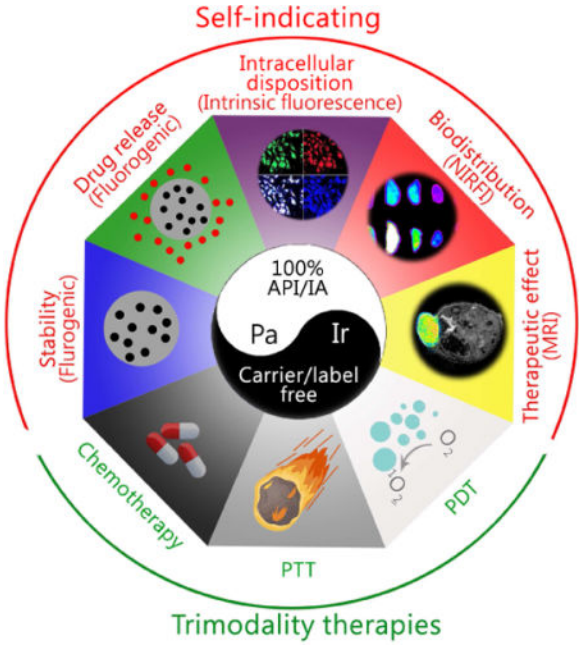

Keywords

Drug delivery; nanoparticles; self-indication; multi-modal therapy; cancer therapy

1. Introduction

Nanoscale drug delivery systems (NDDSs) are engineered nanotechnologies for targeted delivery and controlled release of active pharmaceutical ingredients (APIs).[1–3] So far, conventional NDDSs still suffer from the drawback of low drug loading capacity (%DL[4], generally below 20 wt%[5–7]). A majority part of costly and potentially toxic excipients were employed as carriers to deliver minority part of APIs. One-component nanomedicine[8–10] and drug-drug amphiphiles [11–13] were developed with higher DL%. However, most of them were designed for chemotherapy only, with less imaging and multi-modal therapeutic features. Furthermore, chemotherapy alone may not be very efficient to inhibit highly aggressive or drug-resistant tumors. Non-invasive phototherapies, including photothermal therapy (PTT) and photodynamic therapy (PDT), were reported to synergize chemotherapy and could overcome the drug-resistance through non-overlapping cancer-killing mechanisms.[14, 15] The phototherapeutic agents responsible for reactive oxygen species or heat generation are intrinsically non-toxic, but could be therapeutically effective upon activation with incident light, and thus enable to accurately and controllably ablate a confined area. Therefore, a combination of phototherapy and chemotherapy may achieve precise and more efficient tumor treatment. [16–18] The biological behaviors of conventional NDDSs remained mysterious after fulfilling the drug delivery mission, since they were not typically traceable. To make NDDSs traceable, exogenous imaging agents may be introduced. Yet this necessitates further controls and uncertainty, given that

introduced imaging agents may only indicate their own biological distributions, as it is typically unknown whether they were leaked or detached from the carriers.

We believe the ideal NDDS should meet the following criteria: i) *Drug delivery*: The building blocks are capable to self-assemble into well-defined nanostructures for targeted drug delivery; ii) *High %DL*: Maximizing %DL leads to decreased amount of excipients, thereby decreasing unnecessary toxicity and cost of production; iii) *Self-indication*: The NDDSs, themselves should be engineered with intrinsic imaging features, such that their true biological behaviors can be visualized without additional imaging tags; iv) *Therapeutic efficacy and/or synergistic effect*: The %DL, and thus efficacy, are maximized when the nanocarrier is also the drug, or the carrier and encapsulated API could achieve certain type of synergistic effect.

Hence, we have designed a fully active pharmaceutical ingredient nanoparticle (FAPIN), which was composed of 100% APIs and 100% imaging agents (IA), making FAPIN particularly suitable for trimodality therapies (PTT, PDT and chemotherapy) and intrinsic self-indication. To realize these integrated features, two fluorescent APIs were employed: i) a porphyrin derivative, pheophorbide A (Pa), serving as a hydrophobic building block, and ii) irinotecan (Ir, Camptosar®) as a hydrophilic segment. Pa has been extensively adapted in theranostic nanoplatforms, as it could be used for phototherapy, NIRFI and magnetic resonance imaging (MRI).[19, 20] Ir is an anti-neoplastic drug that inhibits DNA topoisomerase II, in effect terminating tumor cell proliferation.[21–23] As illustrated in Scheme 1, PaIr NPs were constructed through a two-step self-assembly approach, and the components comprising PaIr NPs are 100% theranostically active. Furthermore, the unique and intrinsic imaging capability of PaIr NPs allowed sensitive self-indication of their stability, drug delivery, release and the therapeutic efficacy in spatiotemporal manners. In PaIr NPs, an energy transfer relay[24] dominates and inactivates both fluorescences of Pa and Ir. Hence, despite PaIr NPs being composed of two fluorescent molecules, they exhibit no fluorescence. We consider the nano-assembly in this state to be “primed,” given that dual fluorescence inactivation can be invalidated upon application of specific stimuli to generate a dual-color fluorogenic process. Thus, while conventional NDDSs require extra steps to introduce IAs to indicate their biological behaviors, PaIr NPs are intrinsically self-indicating, allowing for real-time monitoring of nanostructure stability, cellular deposition, drug release and *in vivo* biodistributions. Moreover, PaIr NPs have intrinsic capability to chelate metal ions, such as Mn^{2+} for MRI to assess their treatment outcomes non-invasively. PaIr NPs could preferentially accumulate in tumor sites in patient-derived xenograft (PDX) mice after i.v. administration, due to the enhanced permeability and retention (EPR) effect. [25, 26] and could be activated for synergistic trimodality therapy by laser illumination. PaIr NPs represent a 100%-API based NDDS that were constructed with minimal materials, but exceptionally realized the most diverse theranostic functionalities.

2. Materials and Method

2.1. Materials and characterization

Irinotecan hydrochloride was purchased from BIOTANG Inc. (MA, USA). Pheophorbide A was bought from Santa Cruz Biotechnology. N,N′-Dicyclohexylcarbodiimide (DCC), 4-

(Dimethylamino)pyridine (DMAP), 2′,7′-Dichlorofluorescin diacetate (DCF-DA), $MnCl_2$ and all solvents were purchased from Sigma-Aldrich (MO, USA). Lysotracker™ Green DND-26, singlet oxygen sensor green and CellROX were purchased from Thermo Fisher Scientific Inc. Cell cultures medium, fetal bovine serum, cell cultures dishes and plates were purchased from Corning Inc., USA. PDX GBM tumor tissues were kindly provided by Dr. David James's lab in Neurological Surgery at the University of California, San Francisco. The synthetic compounds were analyzed by Bruker UltraFlextreme MALDI-TOF-MS and 600 MHz Avance III NMR Spectrometer (Bruker, German). The morphology of FAPIN was observed by transmission electron microscopy (TEM, Philips CM-120) with 80 kV acceleration voltage. The cell level laser treatments were conducted by a laser panel (Omnilux new-U) with broad coverage area. *In vitro* fluorescence images were captured by confocal laser scanning microscopy (CLSM, LSM810, Carl Zeiss). The magnetic resonance imaging (MRI) was conducted by Biospec 7T MRI instrument (Bruker, German)

2.2. Synthesis of pheophorbide A and irinotecan conjugate (PaIr)

Pheophorbide A (300 mg, 0.48 mmol) and DCC (120 mg, 0.58 mmol) were dissolved in 6 mL anhydrous dichloromethane, the mixture was stirred at 0°C for 30 min. Then, 359 mg irinotecan hydrochloride (0.58 mmol) and 14.2 mg DMAP (0.116 mmol) were added into the reaction system. The resulting solution was stirred at ambient temperature for 48 h (in dark place). The reaction mixture was filtered and concentrated by rotavapor. The PaIr conjugates were purified by column chromatography by using dichloromethane/methanol (10:1, *vol/vol*) as eluent.

2.3. Preparations and characterizations of PaIr nanoparticles (PaIr NPs)

The PaIr NPs were self-assembled by re-precipitation method. 1 μL PaIr stock solution (100 mM in DMSO) was dropped into 999 μL Milli-Q water under sonication. After 5 s vortex, 100 μM PaIr NPs were fabricated. The size distributions and polydispersity index (PDI) of nanoparticles were evaluated by a dynamic light scattering instrument (Zetasizer, Nano ZS, Malvern, UK). The morphology of NPs was observed by TEM. To prepare TEM sample, the aqueous nanoparticle solution (50 μM) was dropped on copper grids and naturally dried under ambient temperature.

2.4. Preparation of manganese (II) (Mn^{2+}) chelated PaIr NPs

Mn^{2+} chelation process was performed based on the method published previously.[27] Briefly, 23.2 mg PaIr conjugates (20 μmol) and 12.6 mg $MnCl_2$ (100 μmol) were dissolved in 1 mL methanol (with 100 μL pyridine), and refluxed for 2 h. The reaction system was then cooled to room temperature, the un-chelated Mn^{2+} ($MnCl_2$) was removed by extraction (dichloromethane/water). The Mn^{2+} chelated PaIr conjugates distributed in dichloromethane and were dried with a rotavapor. The Mn^{2+} chelated PaIr NPs were made by the method described in section 2.3.

2.5. The relative fluorescence quantum yields of Pa and Ir in PaIr NPs

The relative fluorescence quantum yields were calculated as previously described [28], following the equation:

$$\Phi_{F,x}=\Phi_{F,\mathrm{ref}}\frac{\eta_x^2 I_x A_{\mathrm{ref}}}{\eta_{\mathrm{ref}}^2 A_x I_{\mathrm{ref}}}$$

In the Equation, "Φ_F" denotes the quantum yield. For irinotecan, quinine sulfate in 0.1 N H_2SO_4 was set as a reference. The quantum yield of quinine sulfate is 54.6%.[29] For Pa, Pa in EtOH was set as a reference (Φ_F is 28%).[30] "η" is the refractive index of the solvent, "I" is the integrated fluorescence intensity and "A" is the absorbance at the excitation wavelength. "*ref*" denotes the standard fluorescent dye with known quantum yield, and "x" is the compound that needs to be tested.

2.6. Preparation of Pa/Ir physical mixture for in vivo study

The Pa and Ir are both difficult to dissolved aqueous solvent. For the *in vivo* study, we dissolved Pa or Ir DMSO solution respectively, then dropped them into saline and mixed together (the percentage of DMSO was less than 0.5%). Then, the Pa/Ir mixture was sonicated for 30 min, so that the sediments can be maximally smashed and homogenized. The Pa/Ir mixture needed to be freshly prepared every time before being administrated to the mice. The ultra-small sediments didn't show obvious side effect to the mice.

2.7. Critical aggregation concentrations (CAC) assessment

Pyrene ratiometric method was employed to determine the CAC value of PaIr NPs. Briefly, 999 μL of different concentrations of PaIr NPs were prepared, and 1 μL of 0.1 mM pyrene solution (in acetone) was introduced to PaIr NPs solution and yielded 0.1 μM pyrene solution. The PaIr NPs and pyrene contained solutions were then transferred to a 96-well plate and incubated at 37°C for 2 h. After incubation, the fluorescence of pyrene in each well was evaluated by a microplate reader (excitation is 335 nm). The I_3/I_1 values were recorded for CAC assessment.

2.8. In vitro near-infrared fluorescence (NIRF), reactive oxygen species (ROS) and photothermal evaluation

For NIRF assessment, PaIr monomer or PaIr NPs were dropped on a transparent film and applied to a Kodak multimodal imaging system (excitation at 625±20 nm, emission at 700±35 nm). The ROS productions were indicated by singlet oxygen sensor green (SOSG). Briefly, different concentrations of PaIr NPs or PaIr monomer were incubated with SOSG, and the working solution was exposed to 680 nm laser (0.3 w/cm^2) for 3 min. The fluorescence of SOSG was monitored to indicate the ROS production. For photothermal assessment, different concentrations of PaIr NPs or PaIr monomer were placed in 96-well plate and exposed under 680 nm laser (0.3 w/cm^2) for 3 min. The temperature changes were recorded by FLIR thermal camera. In these experiments, PaIr monomer was prepared by dissolving PaIr molecules in DMSO.

2.9. Stability studies of PaIr NPs

PaIr NPs was dispersed in water and 10% fetal bovine serum water solution, respectively. The final concentrations of PaIr NPs were set to 50 μM. Then, each solution was kept in cell

culture incubator (5% carbon dioxide and 10% humidity. Temperature was 37°C). The fluorescence of Pa in PaIr NPs was monitored by fluorescence photospectrometer, and size distributions at each time point were tested by dynamic light scattering to check the stability of PaIr NPs.

2.10. Fluorescent indication of the accumulated drug release

Two parallel groups of 50 μM PaIr NPs (300 μL) were placed in a 96-well plate. One group was set to neutral pH value (7.4), and another group was in acidic pH (5.0). Each group was assigned to three laser (680 nm) treatments: no laser, low laser power (0.4 w/cm^2), and high laser power (0.8 w/cm^2) doses. The samples were exposed to the intermittent laser, each time point denoted a 3 min laser treatment, followed by a 12 min interval without laser (to allow the sample cooling down to room temperature). The drug release of the 13th time point was tested at 24 h after the 12th laser treatment. The accumulated drug release of PaIr NPs was fluorescently indicated by measuring the fluorescence of released Ir, since only free Ir showed the fluorescence due to the inactivation of energy transfer relay. To avoid the potential FRET caused Ir fluorescence quench, the percentages of drug release were calculated by using the fluorescence of released Ir divided the fluorescence of Ir in Pa/Ir mixture (in the same concentration). To avoid the volume loss, 1 μL fresh PaIr NPs was added to the treated group immediately after we drew 1 μL samples.

2.11. Evaluation of in vitro antitumor activities

U87-MG cells were purchased from the American Type Culture Collection (ATCC, Manassas, VA, USA). Cells were cultured in RPMI 1640 medium supplemented with 10% fetal bovine serum, 100 U/mL penicillin G, and 100 mg/mL streptomycin in a standard cell incubator (37°C with 5% CO_2, and 10% humidity). Cell viabilities were determined by MTS method. U87-MG cells were seeded in 96-well plate with a density of 5000 cells per well. The cells were incubated overnight until fully attached and treated with different concentrations of Pa, Ir, Pa/Ir mixture and PaIr NPs. 12 h later, the extracellular materials were washed off with PBS and replaced with fresh medium. Laser treated group were exposed to the laser (630 nm laser panel) for 3 min, and further incubated with non-laser treated cells for another 24 h. MTS Assay Kit was then added to each well and further incubated for 2 h. The UV-vis absorbance at 495 nm with a reference wavelength of 630 nm was recorded for cell viability assessment. Untreated cells in the medium were employed as controls. Results were shown in form of average cell viability [$(OD_{treat} - OD_{blank})/(OD_{control} - OD_{blank}) * 100\%$] of triplicate wells.

2.12. Intracellular drug release indicated by the dual-color fluorogenic process

Two sets of U87-MG cells were seeded in glass-bottom dishes and treated with 10 μM PaIr NPs for 2 h, respectively. Then the PaIr NPs contained medium was washed off with PBS and replaced with fresh medium. The laser treated group was exposed under 680 nm laser (0.2 w/cm^2) for 1 min, and the intracellular fluorescence of Pa and Ir was monitored by CLSM at different time points. The control groups were not treated with laser, but observed under CLSM at the same time points of their laser treated counterparts. Cy5.5 channel was applied to capture the fluorescence of Pa while DAPI channel was used for that of Ir.

2.13. Lysosome co-localization

U87-MG tumor cells were treated with 10 μM PaIr NPs for 2 h, and then the NPs contained medium was then washed off and replaced with fresh medium. The cells were treated with 680 nm laser (0.2 w/cm^2) for 1 min, and further cultured for another 21.5 h. After that, Lysotracker Green was employed to stain the lysosomes for 0.5 h. The subcellular distributions of Pa, Ir and Lysotracker were recorded by CLSM. The co-localization efficiency was calculated by ImageJ, and depicted in form of Pearson's correlation co-efficiency. Three sets of CLSM micrographs were calculated. For Lysotracker green, FITC channel was used.

2.14. In vitro assessment of reactive oxygen species (ROS) production

Two groups of U87-MG cells were incubated with 10 μM PaIr NPs for 2 h respectively, and then the PaIr NPs contained medium was washed off by PBS and replaced with fresh medium. The DCF-DA was introduced to indicate ROS production. The non-laser treated cells were kept in dark, and the laser-treated cells were exposed to the laser (630 nm laser panel) for 1 min. The cells were collected for flow cytometry analysis. Cy5.5 channel was applied to indicate Pa while FITC channel was used for that of DCF-DA.

2.15. CLSM observations of laser-guided cell death

U87-MG cells were incubated with 10 μM PaIr NPs in glass-bottom dishes. 2 h later, the PaIr NPs contained medium was washed off and replaced with fresh medium. Then, an incident laser (680 nm, 0.2 w/cm^2 for 3 min) was shining to a specific region of the cells. After the laser treatment, cells were stained with 40 nM of DiOC6(3) to indicate the mitochondrial membrane potential (Live cells), and propidium iodide (PI) was employed to stain the dead cells. The live and dead cells were visualized by CLSM. Non-PaIr NPs treated cells were employed as control (treated with identical laser exposure and staining procedures).

2.16. Establishment of patient-derived xenograft (PDX) GBM-bearing mice models

Male athymic nude mice (6~8 weeks) were purchased from Harlan (Livermore, CA, USA). All animal experiments were strictly in compliance with the guidelines of Animal Use and Care Administrative Advisory Committee of University of California, Davis. The PDX GBM-bearing mice models were established by inoculated PDX GBM (12FLR) tissues subcutaneously to the flank of the nude mice.

2.17. In vivo photothermal therapy

PaIr NPs was i.v. administrated into tumor-bearing mice (n=6). 24 h and 48 h after the i.v. injection, the tumor regions were exposed to 680 nm laser with low (0.4 w/cm^2) and high (0.8 w/cm^2) power for 3 min. Pa/Ir mixture and PBS group were treated with high dose laser (3 min) as control group. The laser-induced hyperthermia was recorded by FLIR thermal camera.

2.18. Ex vivo assessment of ROS production

PBS, Pa/Ir mixture and PaIr NPs were i.v. administrated into tumor-bearing mice (n=3). 24 h later, the mice were sacrificed, and the tumors were collected. The collected tumors were imaged by Kodak multimodal imaging system to get the “pre-CellROX” images. Then, the tumors were applied to laser treatments (680 nm, 3 min). The tumors from PaIr NPs treated mice were exposed to high (0.8 w/cm^2) and low (0.4 w/cm^2) laser, respectively. As control groups, the tumors from PBS and Pa/Ir mixture groups were treated by 0.8 w/cm^2 laser. After laser treatments, the tumors were immediately doused into ROS probe (CellROX® Deep Red) working solution for 15 s. Then, the tumors were scanned on a Kodak multimodal imaging system to get the “post-CellROX” images. In order to exclude the fluorescence interference from Pa, the ROS productions were calculated by “post-CellROX” deducted the “pre-CellROX” readouts. CellROX® Deep Red is a fluorogenic dye, which exhibits strong NIRF in the presence of ROS.

2.19. Ex vivo near infra-red fluorescence imaging (NIRFI)

Pa/Ir mixture and PaIr NPs were i.v. administrated into the mice with two PDX tumors at both flanks. The tumor on the left side was exposed to the laser (680 nm, 0.4 w/cm^2) for 3 min, the right tumor was not treated with laser. The fluorescence of Pa was imaged by a Kodak multimodal imaging system to indicate the organ distributions of PaIr NPs. Excitation was 625 ± 20 nm, and emission was 700 ± 35 nm.

2.20. In vivo evaluations of therapeutic efficacy

PDX GBM-bearing mice were employed for *in vivo* therapeutic efficacy evaluation. The mice were randomly assigned into 6 groups (n=6) to receive the following treatments: i) PBS; ii) free Ir; iii) Pa/Ir mixture (with high laser dose); iv) PaIr NPs without laser; v) PaIr NPs (with low laser dose); vi) PaIr NPs (with high laser dose). All materials were i.v. administrated through the tail vein once per week. 24 h and 48 h after the materials administration, tumors of the laser treated groups were exposed to 680 nm laser for 3 minutes to elicit the chemo-, photodynamic- and photothermal- therapeutic effect. The variations of tumor size and body weights of all mice were recorded during the treatment. Survival cut-off criteria included tumor ulceration or compassionate euthanasia, when the tumor size was more than 1000 mm^3 in volume, or if the tumor impeded eating, urination, defecation or ambulation.

2.21. In vitro and in vivo MRI

For cellular level MRI, U87-MG cells were incubated with different concentrations of Mn^{2+} chelated PaIr NPs for 2 h. Then, the cells were fixed in agarose gel and scanned by Bruker Biospec 7T MRI scanner using T1-weighted Multi-Slice Multi Echo (MSME) sequence (echo time (TE)/repetition time (TR) 14/500 ms) with 128*128 matrix size. For *in vivo* MRI studies, Mn^{2+} chelated PaIr NPs (Mn^{2+} dose: 0.015 mmole/kg) were i.v. administrated into PDX GBM-bearing mice, the mice were then imaged by using a T1-weighted Multi-Slice Multi Echo (MSME) sequence on a Bruker Biospec 7T MRI scanner (TE/TR 14/500 ms) with 512*512 matrix size.

2.22. Data statistics

Data statistics were analyzed by calculating the *t-test* between two groups, and One-way ANOVA analysis of variations for multiple groups. Unless otherwise noted, all results were expressed as the mean ± s.d. A value of $p<0.05$ was considered statistically significant.

3. Results and Discussion

3.1. Fabrication and characterization of PaIr NPs

PaIr monomers were synthesized by covalently conjugating two commercial available APIs through ester bond (Figure 1a). Their molecular weight and compositions were confirmed by mass spectrometry and nuclear magnetic resonance (NMR) as shown in Figure S1~S4. PaIr monomers were then assembled into PaIr NPs through re-precipitation method.[31–33] The size of PaIr NPs was around 88 nm, with a PDI of 0.167, suggesting the nanoparticles were well-dispersed (Figure 1b). The surface charge of the PaIr NPs was 30.9 mV (Figure S5). TEM micrographs (Figure 1c) showed that the PaIr NPs were in spherical morphology, within which revealed many small dark dots. We believe these dots were micelle-like assemblies of PaIr monomers, which in turn self-assembled into larger nano-aggregates through multi-micelle aggregation as previously reported [11, 34, 35]. This proposed self-assembly process was illustrated in Figure S6. PaIr monomers were self-assembled into small micelles-like architecture, due to their amphiphilic chemical structures. The small PaIr micelle-like architecture then further aggregated into larger nanoparticles through multi-micelle aggregation that may be driven by "**π**~**π**" stacking interaction among the big planar structure of Ir. The critical aggregation concentration (CAC) [36] of PaIr NPs was determined to be 1 μM (Figure S7). The UV-vis spectra (Figure 1d) showed that PaIr monomers exhibited all peaks of Pa, plus a distinguishable shoulder on the left of Pa's 412 nm peak. As this shoulder overlapped with 370 nm peak of Ir, indicating that PaIr monomers were composed of both Pa and Ir.

3.2. Fluorescence properties of PaIr NPs

The fluorescence properties of Pa, Ir, PaIr monomers and PaIr NPs were investigated. In Figure 1e, Pa and Ir exhibited fluorescence peaks centered at 690 and 430 nm, respectively. When excited at 370 nm, the fluorescence intensity of PaIr monomer at 430 nm (Ir emission) was ~20 times decreased in comparison to equimolar Ir, but showed a slight enhancement at 690 nm (Pa emission), compared to that of Pa at same concentrations. This could be explained by that Ir (donor) transferred its emissive energy to excite Pa (acceptor), which was enabled due to the spectral overlap between Ir and Pa (Figure 1f) and was further proved by energy transfer verification studies shown in Figure S8.

In PaIr NPs, neither Ir (Figure 1e) nor Pa (Figure 1g) was fluorescently detectable. Their fluorescence was largely quenched. The quantum yield of Pa was measured to be 0.03%, and the Ir was 0.6%. Ir quenching was ascribed to energy transfer, and Pa quenching was hypothetically conceived as aggregation-caused quenching (ACQ).[37, 38] The assembly of planar Pa molecules structures leads to efficient "**π**-**π**" stacking, and therefore fluorescence quenching. To test this experimentally, PaIr monomers were suspended in a mixed solvent to realize diverse aggregation states (Figure 1h). PaIr monomers showed strong fluorescence

when dissolved in pure DMSO, but gradually decreased as the water fraction (f_w) increased, finally yielded ~83 times fluorescence quench (Figure 1i). Hence, the fluorescence inactivation of Pa was ascribed to ACQ in PaIr NPs. We concluded that an energy transfer relay occurred in PaIr NPs (Figure 1j), i.e. Ir transferred its emissive energy to Pa, and Pa quenched both fluorescences from transfer energy and itself by ACQ. This unique fluorescence property was highly useful to indicate nanostructure stability or drug release in response to a specific stimulus (laser or acid pH), as these responses would make the energy transfer relay invalid, and enabled generation of a dual-color fluorogenic process. Furthermore, the recovery of each fluorescence could indicate different *in vitro* or *in vivo* processes, for instance, the recovery of Ir fluorescence could indicate drug release, while Pa fluorescence reported on the dis-/assembly of the NPs, and both types of fluorescence unveiled the true biological behaviors of PaIr NPs.

3.3. Investigation of NIFRI, photodynamic- and photothermal- effects

We further investigated the NIRFI capability of PaIr NPs (Figure 2a). PaIr NPs fluorescence was mostly inactivated, even at an increased concentration. Oppositely, the fluorescence of dispersed PaIr was enhanced along with increasing concentrations. Thus the fluorescence imaging results were in agreement with the fluorescence measurements (Figure 1g). The “ON” and “OFF” of the Pa fluorescence could indicate the integrity of PaIr assemblies. Then, the photothermal effects were measured (Figure 2b). PaIr NPs comparatively generated more heat than their dispersed counterparts. This may be ascribed to the restrictions in molecular motion associated with assembly into nanostructures, most photo-energy is transformed into heat, rather than being absorbed by typical intramolecular motions, such as those dominating energy displacements in PaIr monomers. The photothermal effects increased with concentration (Figure 2c). The photodynamic effects were shown in Figure 2d, the dispersed PaIr showed higher ROS generation than the nano-formulation.

3.4. Fluorescent self-indication of stability

As self-indicating NDDS, PaIr NPs enabled to fluorescently indicate their own stability. As shown in Figure S9a, the fluorescence of Pa, both in water and 10% serum, didn’t show significant variations for more than a week, the persistent ACQ indicated that the PaIr NPs kept in assembled state. The size of PaIr NPs was also monitored by DLS (Figure S9b). PaIr NPs in water and serum both didn’t exhibited large size variations after a week, which was consistent with fluorescence results. In 10% serum, PaIr NPs was slightly bigger than that in water. The size increments were hypothetically ascribed to the formation of a protein corona, [39, 40] which typically occurs for nanoparticles administered in biological systems. However, the size of PaIr NPs showed no obvious changes even following incubation with serum for 1 month (Figure S10), indicating their excellent stability.

3.5. Fluorescent self-indication of drug release

PaIr NPs were constructed with a photosensitizer and a chemotherapeutic drug via an ester bond. They were intentionally designed for laser/acid pH-triggered drug release. Laser could be used to irradiate the photosensitizer, while the acidic pH enables hydrolyzation of the ester bond, both facilitating the drug release from PaIr NPs. In self-indicating PaIr NPs, the

fluorescence recovery of Ir can directly indicate drug release, as the detachment of Ir from NPs would invalid the energy transfer. Before applying the laser to NPs, laser doses were optimized by evaluating photothermal effects (Figure S11). The photo-induced temperature enhancements increased from 14°C (0.2 w/cm^2) to 49°C (1.0 w/cm^2), indicating higher laser power, more heat generation. We then chose values for a low and high laser dose for the following phototherapy evaluations, 0.4 w/cm^2 and 0.8 w/cm^2, respectively. PaIr NPs were dispersed in aqueous solutions varying in pH (pH 7.4 and pH 5.0) and exposed under laser. As shown in Figure 2e, in neutral pH, PaIr NPs released fewer Ir without laser, but exhibited increased drug release upon continuous laser exposure. Ir release correlated with the level of laser power. In acidic pH, the Ir release was dramatically expedited, thus the fluorescence of Ir was higher than their corresponding groups at neutral pH. PaIr NPs drug release reached the highest level (almost 80%) when both high laser and acidic pH were used, surpassing the drug released triggered by a single stimulus. Figure 2f displayed fluorescent images of the Ir after the release experiments. In the presence of both laser and acidic pH, the blue fluorescence of Ir was markedly higher than their untreated counterparts. The laser treatment enabled to largely expedite the drug release. We hypothesized that the incident laser could be transferred to molecular motions, such as molecular vibration, movement or rotation, which would be destructive to the nanostructure. Moreover, the photo-induced hyperthermia could intensify the Brownian movement of PaIr molecules, and further expedite the disassembly of the nanostructures. Once the nanostructures were collapsed, the ester bond gained more chances to react with an acidic environment, resulting in more efficient drug release. The observed drug releasing patterns suggested that PaIr NPs could undergo laser triggered chemotherapy for cancer treatment *in vivo*, and furthermore, this drug release would be further increased in the acidic microenvironment of solid tumors.

3.6. Synergistic therapeutic effects of phototherapy and chemotherapy

U87-MG cells were incubated with PaIr NPs for evaluation of *in vitro* anti-tumor efficacy (Figure 2g). Pa alone exhibited less cytotoxicity without laser treatment. Treatments with Ir, Pa+Ir, and PaIr NPs exhibited cytotoxicity, but not with high efficacy, considering that they all contained the chemotherapeutic drug. Upon laser exposure (Figure 2h), Pa exhibited distinguishable efficacy, while Pa+Ir yielded more efficient therapeutic effect compared to Pa or Ir alone. Thus, the improved efficacy may be ascribed to a combination of phototherapies and chemotherapy. PaIr NPs exerted the most efficient effect than the other three groups, reaching an IC_{50} of ~0.5 μM, which was 10 times lower than that of Pa+Ir (~5 μM), and 60 times than that of Pa (~30 μM). The high efficacy of PaIr NPs was not only provided by the synergistic effect (Figure 2i) of phototherapy and chemotherapy (Combination index of all concentrations were below 0.1), but may also be attributed to the enhanced intracellular drug delivery by nanoparticles.[41, 42] The overwhelming therapeutic effects suggested that irradiation not only triggered the phototherapies, but may have also triggered the drug release, thus activating the chemotherapeutic effect.

3.7. In vitro ROS production

In vitro photodynamic effect was then evaluated by fluorescence-activated cell sorting (FACS) in Figure 2j. Control U87-MG cells produced little ROS under laser exposure, PaIr NPs treated cells exhibited very striking ROS production under laser (Q2 increased from

1.32% to 22.4%), indicating that PaIr NPs exhibited excellent PDT in cell level. We then irradiated a discrete area of cells pre-incubated with PaIr NPs and comparatively assessed cell death between the laser exposed region and non-laser treated cells (Figure 2k). Cells exposed to laser were mostly dead. In comparison, cells not directly exposed to laser (but containing PaIr NPs) did not exhibit obvious cell death. The PBS control group did not show obvious cell death, even with laser treatment. These results supported that PaIr NPs may allow for highly controllable and accurate therapeutic effect, i.e., only in particular regions where the laser was directed.

3.8. Cellular drug release and distribution indicated by intrinsic fluorescence

To further exploit the drug release at cellular level, we incubated U87-MG cells with PaIr NPs, and observed the dual-color fluorogenic process in a spatiotemporal manner (Figure 3a). Prior to laser irradiation, neither the Pa nor Ir could be fluorescently distinguished. In non-laser treated group, the cells yielded an increase in Pa fluorescence, but very weak Ir fluorescence (24 h). In contrast, the laser treated group exhibited remarkable fluorogenic subsequences of both Pa and Ir and showed significantly fluorogenic differences with their non-laser treated counterparts (Figure 3b). The subcellular distributions of Pa and Ir were colocalized in certain regions, indicating PaIr NPs may release Ir at localized intracellular sites. Since nanoparticles were generally taken up by cells via endocytosis pathway and subsequently transported to endosomes/lysosomes,[43, 44] the brighter regions may denote the locale of lysosomal compartments. Therefore, we co-stained PaIr NPs treated cells with lysosomes tracker and calculated the lysosomes colocalization efficiency [45, 46] (Figure 3c and 3d). The fluorescence of Pa, Ir and lysosomes were largely colocalized and showed high colocalization efficiency (more than 0.9), indicating that the microenvironment of lysosomes may assist the drug releasing, such as low pH value (~5.0). The subcellular drug releasing behaviors were consistent with the laser/pH co-stimulated drug releasing results (Figure 2e and 2f), and supported that PaIr NPs responded to both external (laser) and internal (acidic pH) stimuli, thus enabling highly controllable cancer treatments.

3.9 Animal study procedures

Glioblastoma multiforme (GBM) is an aggressive type of primary brain tumor with very poor prognosis.[47–49] Therefore, we evaluated PaIr NPs on patient-derived xenograft (PDX) model of GBM (12FLR). As illustrated in Figure S12, the mice were randomly assigned into 6 groups (n=6): PBS control, Ir, PaIr NPs without the laser, Pa+Ir with high dose laser (Pa+Ir H), PaIr NPs with high dose laser (PaIr NP H) and low dose laser (PaIr NPs L) groups. Two doses of each material were i.v. administrated on the first day of two consecutive weeks. Pa containing groups were treated by laser after 24 and 48 h of injection, at which point the photothermal effect was recorded by thermal imaging. Tumor volumes and body weights were measured throughout the experiments.

3.10. Ex vivo biodistribution of PaIr NPs indicated by NIRFI

The biodistribution of PaIr NPs could be indicated by their intrinsic NIRF (Figure 4a and 4b). In the group treated with PaIr NPs, most organs showed very low fluorescence signal. The NIRF at liver and lung was relatively high, likely due to the opsonization[50, 51], but it was much lower than Pa+Ir mixture treated group. NIRF on both tumors suggested that PaIr

NPs could preferentially accumulate in the tumor. The laser treated tumor exhibited relatively stronger NIRF, implied that the NPs experienced a laser triggered disassembly process, which was beneficial to the drug release. Pa+Ir treated mice exhibited much stronger signal in spleen, liver and lung, but not in tumor (even at laser triggered tumor), indicating that Pa+Ir molecules were mostly transported to reticuloendothelial system for clearance. The accumulation of Pa+Ir in kidney indicated that the small molecules of Pa were possibly excreted from the kidney. As the fluorescence of Pa was both quenched in PaIr NPs. The biodistribution of PaIr NPs was not very accurately indicated by the intrinsic NIRF. We, therefore, employed photothermal/dynamic imaging and MRI to further monitor the tumor accumulation of the PaIr NPs.

3.11. In vivo photo-thermal/dynamic effects

The phototherapeutic effect of Pa+Ir and PaIr NPs was evaluated in mice (n=6) in comparison to PBS control groups. As shown in Figure S13 and Figure 4c, the PaIr NPs H group yielded the significant stronger photothermal effect compared to the other groups ($P<0.01$). The PaIr NPs L and Pa+Ir H generated only very little heat compared to PBS control. The photodynamic effect was shown in Figure 4d and 4e. PBS control group showed minimum ROS production while all the Pa containing groups exhibited excellent photodynamic effect. PaIr NPs H elicited the strongest ROS production, followed by the Pa +Ir and PaIr NPs L treated groups.

3.12. Self-indication of phototherapy outcomes by MRI

PaIr NPs have the intrinsic capability to chelate metal ions, such as Mn^{2+} (Figure 4f). As shown in Figure S14a, the fluorescence of Pa (in dispersed PaIr) was quenched compared to non-chelated counterparts, demonstrating the successful chelation of Mn^{2+}. We then assembled Mn^{2+} chelated PaIr molecules into nanoformulation. The hydrodynamic diameter (Figure S14b) of the Mn^{2+} chelated PaIr NPs was 97 nm, a slightly bigger than non-chelated PaIr NPs. The PDI of the Mn^{2+} chelated PaIr NPs was 0.189, indicating they were well-dispersed in aqueous solution. Figure S14c showed the morphology of the Mn^{2+} chelated PaIr NPs. The Mn^{2+} chelated PaIr NPs stayed in spherical morphology and were assembled by a cluster of small dark dots, which supported that the metal chelation showed less effect on PaIr NPs self-assembly. Figure 4g showed the concentration-dependent r_1 relaxation of PaIr NPs, indicating PaIr NPs were capable of MRI. In Figure S14d, Mn^{2+} chelated PaIr NPs enhanced the T_1 MR contrast of U87-MG cells in a concentration-dependent manner. Mn^{2+} chelated PaIr NPs was further employed as a MRI nanoprobe for *in situ* indications of their *in vivo* delivery and therapeutic efficacy (Figure 4h). The T_1 MRI contrast at tumor site started to increase 2 h post-injection, and became significantly higher at 24 h. Tumors were then treated twice with laser (0.8 w/m^2) for 3 min at 24 h and 48 h of post-injection. MRI was used to continuously monitor the treatment outcomes. MR image at 72 h showed significant tumor shrinkage and large volume of necrotic tissue at the tumor site. The tumor kept on shrinking with time elapse, and was almost eliminated at 7 days post-injection. In contrast, the PBS group with the same dose of laser did not show any tumor ablation as indicated by MRI (Figure S15).

3.13. In vivo trimodality therapeutic effects

The antitumor efficacy was further evaluated in PDX GBM models (Figure 5a). Due to the highly aggressive and malignant characteristics, PDX GBM in PBS group grew so fast that no mice survived more than 10 days. The free Ir group performed similarly, indicating that the development of PDX tumors could not be effectively inhibited by free chemo-drug. PaIr NPs without laser group also did not perform well with respect to tumor shrinkage. As aforementioned in Figure 2g and 2h, PaIr NPs without laser treatment was less effective than their laser treated counterparts, as neither the phototherapies nor chemotherapy were activated. In Pa+Ir H treated group, the tumor volumes were decreased after two doses of treatments. It should be noted that PaIr NPs H exhibited the best antitumor efficacy among all the groups. The tumors volume was significantly decreased after the first dose, and kept on shrinking as time elapsed. Furthermore, PaIr NPs with low laser dose (showed the similar photothermal effect to PBS, Figure 4c) was employed to evaluate the efficacy of PDT and chemotherapy to avoid these two therapeutic effects being overwhelmed by the dominant PTT effect at high laser dose. PaIr NPs L group possessed similar therapeutic efficacy as PaIr NPs H treatment, indicating that the combinations of chemo- and photodynamic therapies played a key role in tumor treatment. The survival rate of PaIr NPs H and PaIr NPs L was higher than other groups (Figure 5b). Interestingly, three mice were completely cured in the PaIr NPs H group and these animals survived over 2 months. The PaIr NPs L group also showed excellent efficacy, given that two mice were completely cured following treatment. The tumor images for each group after two doses of treatments were displayed in Figure 5c. Similar to the large tumors in groups treated with PBS and Ir, those in PaIr NPs treated mice with no laser irradiation showed only slight shrinkage. In contrast, each of the laser treated groups achieved obvious tumor ablation. Pa+Ir H treated tumors showed an initial response (Figure 5c), but relapsed near the scar. PaIr NPs L treated mice showed only slight scar, since the PTT effect was not as effective as its high laser dose counterparts. The low relapse rate of PaIr NPs laser treated groups may be ascribed to the complementary chemotherapy. The released Ir may continuously provide a chemotherapeutic effect during the post-phototherapy period, and thus prevent tumor relapse. 33.3% mice (2 of 6) in PaIr NPs L in and 50% mice in PaIr NPs H (3 of 6) were completely cured (Figure 5d). Every cured mouse lived in excellent quality and the tumor scar fell off naturally (the cured regions are circled in red), no palpable tumors were observed in two months.

The PaIr NPs treated tumor tissue was then investigated by hematoxylin and eosin (H&E) stain (Figure 5e). Microscopically, the PaIr NPs mediated light therapy caused massive tissue pathological changes, including edema, cellular disassociation and shrinking, pyknosis and karyolysis. Comparatively, the tumor tissue of PBS with laser group showed no damage, suggesting that laser alone did not obviously damage the tissue. Thus H&E staining supported that PaIr NPs exhibit excellent phototherapeutic effects that enable the targeted demolition of tumor tissues.

3.14. Systemic toxicity evaluations

No significant body weight changes among all treatment groups were observed, indicating minimal systemic toxicity (Figure 5f). The pathology of the major organs of PaIr NPs treated mice showed identical patterns compared to PBS control group (Figure 5g). The

hematologic index did not suggest any abnormal alterations after treatments (Figure S16). All results suggested that PaIr NPs did not show obvious systemic toxicity, and therefore warranted further clinical developments.

4. Conclusions

In this work, we reported a self-indicating, fully active pharmaceutical ingredients nanoparticle (FAPIN) by using minimal materials, but possessing a variety of unique properties: i) 100 % API/IA loading, and being self-delivered (carrier-free) and self-indicated (label-free); ii) the nanoparticle stability (Figure S9) and iii) drug releasing pattern (Figure 2e and 2f), even at cellular level (Figure 3a and 3b) could be self-indicated by the unique dual-color fluorogenic process; iv) the subcellular dispositions of NPs were self-indicated by intrinsic fluorescence (Figure 3c); v) the organs distributions were self-indicated by NIRF (Figure 4a and 4b); vi) the therapeutic effect could be self-indicated by MRI (Figure 4h); vii) powerful trimodality therapies. PaIr NPs with laser exposure exhibited ~10 times lower IC_{50} than Pa+Ir and ~60 times than single photosensitizer (Figure 2h), and 50% mice were completely cured with no relapse in 2 months (Figure 5a~5d). FAPIN achieved nanoscale integration of imaging and trimodality therapy, and demonstrated multifunctional theranostic benefits and their synergistic effect in a combined approach. The PaIr NPs could be laser-activated for PDT, PTT and chemotherapy simultaneously in a controllable manner, and the intrinsic synergistic mechanisms of the trimodality therapy within one nano-formulation further enhanced the therapeutic efficacy. The phototherapy may suffer from low light penetration. For tumors that are beyond the reach of the light, antitumor effects can still be achieved with PaIr NPs by releasing chemotherapeutic drug. This integrated yet easy-to-make FAPIN nanomedicine platform shows great promise as highly versatile, controllable, low-cost, multimodal theranostic nano-agents against cancers.

Supplementary Material

Refer to Web version on PubMed Central for supplementary material.

Acknowledgments

We thank Dr. Sonal Desai for the editorial help and the financial support from NIH/NCI (R01CA199668), NIH/NICHD (R01HD086195) and UC Davis Comprehensive Cancer Center Support Grant (CCSG) awarded by the National Cancer Institute (NCI P30CA093373).

References

1. Peer D, Karp JM, Hong S, Farokhzad OC, Margalit R, Langer R. Nanocarriers as an emerging platform for cancer therapy. Nat Nanotech. 2007; 2(12):751–760.
2. Qin SY, Zhang AQ, Cheng SX, Rong L, Zhang XZ. Drug self-delivery systems for cancer therapy. Biomaterials. 2017; 112:234–247. [PubMed: 27768976]
3. Song W, Musetti SN, Huang L. Nanomaterials for cancer immunotherapy. Biomaterials. 2017; 148:16–30. [PubMed: 28961532]
4. Ankrum JA, Miranda OR, Ng KS, Sarkar D, Xu C, Karp JM. Engineering cells with intracellular agent–loaded microparticles to control cell phenotype. Nat Protocols. 2014; 9(2):233–245. [PubMed: 24407352]

5. Li Y, Xiao K, Luo J, Xiao W, Lee JS, Gonik AM, Kato J, Dong TA, Lam KS. Well-defined, reversible disulfide cross-linked micelles for on-demand paclitaxel delivery. Biomaterials. 2011; 32(27):6633–6645. [PubMed: 21658763]
6. Zhang CY, Yang YQ, Huang TX, Zhao B, Guo XD, Wang JF, Zhang LJ. Self-assembled pH-responsive MPEG-b-(PLA-co-PAE) block copolymer micelles for anticancer drug delivery. Biomaterials. 2012; 33(26):6273–6283. [PubMed: 22695069]
7. Zhu C, Jung S, Luo S, Meng F, Zhu X, Park TG, Zhong Z. Co-delivery of siRNA and paclitaxel into cancer cells by biodegradable cationic micelles based on PDMAEMA–PCL–PDMAEMA triblock copolymers. Biomaterials. 2010; 31(8):2408–2416. [PubMed: 19963269]
8. Su H, Koo JM, Cui H. One-component nanomedicine. J Control Release. 2015; 219:383–395. [PubMed: 26423237]
9. Wang Y, Cheetham AG, Angacian G, Su H, Xie L, Cui H. Peptide–drug conjugates as effective prodrug strategies for targeted delivery. Adv Drug Deliv Rev. 2017; 110:112–126. [PubMed: 27370248]
10. Andrew MacKay J, Chen M, McDaniel JR, Liu W, Simnick AJ, Chilkoti A. Self-assembling chimeric polypeptide-doxorubicin conjugate nanoparticles that abolish tumours after a single injection. Nat Mater. 2009; 8(12):993–999. [PubMed: 19898461]
11. Huang P, Wang D, Su Y, Huang W, Zhou Y, Cui D, Zhu X, Yan D. Combination of Small Molecule Prodrug and Nanodrug Delivery: Amphiphilic Drug–Drug Conjugate for Cancer Therapy. J Am Chem Soc. 2014; 136(33):11748–11756. [PubMed: 25078892]
12. Ma W, Cheetham AG, Cui H. Building nanostructures with drugs. Nano Today. 2016; 11(1):13–30. [PubMed: 27066106]
13. Cheetham AG, Chakroun RW, Ma W, Cui H. Self-assembling prodrugs. Chem Soc Rev. 2017; 46(21):6638–6663. [PubMed: 29019492]
14. Cheng L, Wang C, Feng L, Yang K, Liu Z. Functional Nanomaterials for Phototherapies of Cancer. Chem Rev. 2014; 114(21):10869–10939. [PubMed: 25260098]
15. Yang X, Liu Z, Li Z, Pu F, Ren J, Qu X. Near-Infrared-Controlled, Targeted Hydrophobic Drug-Delivery System for Synergistic Cancer Therapy. Chem Eur J. 2013; 19(31):10388–10394. [PubMed: 23765904]
16. Chen W, Ouyang J, Liu H, Chen M, Zeng K, Sheng J, Liu Z, Han Y, Wang L, Li J, Deng L, Liu YN, Guo S. Black Phosphorus Nanosheet-Based Drug Delivery System for Synergistic Photodynamic/Photothermal/Chemotherapy of Cancer. Adv Mater. 2017; 29:1603864.
17. Conde J, Oliva N, Zhang Y, Artzi N. Local triple-combination therapy results in tumour regression and prevents recurrence in a colon cancer model. Nat Mater. 2016; 15(10):1128–1138. [PubMed: 27454043]
18. Chen Q, Wang C, Cheng L, He W, Cheng Z, Liu Z. Protein modified upconversion nanoparticles for imaging-guided combined photothermal and photodynamic therapy. Biomaterials. 2014; 35(9): 2915–2923. [PubMed: 24412081]
19. Lovell JF, Jin CS, Huynh E, Jin H, Kim C, Rubinstein JL, Chan WCW, Cao W, Wang LV, Zheng G. Porphysome nanovesicles generated by porphyrin bilayers for use as multimodal biophotonic contrast agents. Nat Mater. 2011; 10(4):324–332. [PubMed: 21423187]
20. Li Y, Lin T-y, Luo Y, Liu Q, Xiao W, Guo W, Lac D, Zhang H, Feng C, Wachsmann-Hogiu S, Walton JH, Cherry SR, Rowland DJ, Kukis D, Pan C, Lam KS. A smart and versatile theranostic nanomedicine platform based on nanoporphyrin. Nat Commun. 2014; 5:4712. [PubMed: 25158161]
21. Vredenburgh JJ, Desjardins A, Herndon JE, Dowell JM, Reardon DA, Quinn JA, Rich JN, Sathornsumetee S, Gururangan S, Wagner M, Bigner DD, Friedman AH, Friedman HS. Phase II Trial of Bevacizumab and Irinotecan in Recurrent Malignant Glioma. Clin Cancer Res. 2007; 13(4):1253. [PubMed: 17317837]
22. Conti JA, Kemeny NE, Saltz LB, Huang Y, Tong WP, Chou TC, Sun M, Pulliam S, Gonzalez C. Irinotecan is an active agent in untreated patients with metastatic colorectal cancer. J Clin Oncol. 1996; 14(3):709–715. [PubMed: 8622015]
23. Kreisl TN, Kim L, Moore K, Duic P, Royce C, Stroud I, Garren N, Mackey M, Butman JA, Camphausen K, Park J, Albert PS, Fine HA. Phase II Trial of Single-Agent Bevacizumab

Followed by Bevacizumab Plus Irinotecan at Tumor Progression in Recurrent Glioblastoma. J Clin Oncol. 2009; 27(5):740–745. [PubMed: 19114704]

24. Xue X, Jin S, Zhang C, Yang K, Huo S, Chen F, Zou G, Liang XJ. Probe-Inspired Nano-Prodrug with Dual-Color Fluorogenic Property Reveals Spatiotemporal Drug Release in Living Cells. ACS Nano. 2015; 9(3):2729–2739. [PubMed: 25688453]
25. Fang J, Nakamura H, Maeda H. The EPR effect: Unique features of tumor blood vessels for drug delivery, factors involved, and limitations and augmentation of the effect. Adv Drug Deliv Rev. 2011; 63(3):136–151. [PubMed: 20441782]
26. Maeda H, Wu J, Sawa T, Matsumura Y, Hori K. Tumor vascular permeability and the EPR effect in macromolecular therapeutics: a review. J Control Release. 2000; 65(1–2):271–284. [PubMed: 10699287]
27. Tam NCM, McVeigh PZ, MacDonald TD, Farhadi A, Wilson BC, Zheng G. Porphyrin–Lipid Stabilized Gold Nanoparticles for Surface Enhanced Raman Scattering Based Imaging. Bioconj Chem. 2012; 23(9):1726–1730.
28. Würth C, Grabolle M, Pauli J, Spieles M, Resch-Genger U. Comparison of Methods and Achievable Uncertainties for the Relative and Absolute Measurement of Photoluminescence Quantum Yields. Anal Chem. 2011; 83(9):3431–3439. [PubMed: 21473570]
29. Eaton DF. Reference materials for fluorescence measurement. Pure Appl Chem. 1988:1107.
30. Eichwurzel I, Stiel H, Röder B. Photophysical studies of the pheophorbide a dimer. J Photochem Photobiol B: Biol. 2000; 54(2):194–200.
31. Kasai H, Murakami T, Ikuta Y, Koseki Y, Baba K, Oikawa H, Nakanishi H, Okada M, Shoji M, Ueda M, Imahori H, Hashida M. Creation of Pure Nanodrugs and Their Anticancer Properties. Angew Chem Int Ed. 2012; 51(41):10315–10318.
32. Yu Y, Feng C, Hong Y, Liu J, Chen S, Ng KM, Luo KQ, Tang BZ. Cytophilic Fluorescent Bioprobes for Long-Term Cell Tracking. Adv Mater. 2011; 23(29):3298–3302. [PubMed: 21671445]
33. Xue X, Zhao Y, Dai L, Zhang X, Hao X, Zhang C, Huo S, Liu J, Liu C, Kumar A, Chen WQ, Zou G, Liang XJ. Spatiotemporal Drug Release Visualized through a Drug Delivery System with Tunable Aggregation-Induced Emission. Adv Mater. 2014; 26(5):712–717. [PubMed: 24129910]
34. Lodge TP, Rasdal A, Li Z, Hillmyer MA. Simultaneous, Segregated Storage of Two Agents in a Multicompartment Micelle. J Am Chem Soc. 2005; 127(50):17608–17609. [PubMed: 16351082]
35. Mai Y, Zhou Y, Yan D. Synthesis and Size-Controllable Self-Assembly of a Novel Amphiphilic Hyperbranched Multiarm Copolyether. Macromolecules. 2005; 38(21):8679–8686.
36. Kalyanasundaram K, Thomas JK. Environmental effects on vibronic band intensities in pyrene monomer fluorescence and their application in studies of micellar systems. J Am Chem Soc. 1977; 99(7):2039–2044.
37. Hong Y, Lam JWY, Tang BZ. Aggregation-induced emission: phenomenon, mechanism and applications. Chem Commun. 2009; (29):4332–4353.
38. Hong Y, Lam JWY, Tang BZ. Aggregation-induced emission. Chem Soc Rev. 2011; 40(11):5361–5388. [PubMed: 21799992]
39. Salvati A, Pitek AS, Monopoli MP, Prapainop K, Bombelli FB, Hristov DR, Kelly PM, Aberg C, Mahon E, Dawson KA. Transferrin-functionalized nanoparticles lose their targeting capabilities when a biomolecule corona adsorbs on the surface. Nat Nanotech. 2013; 8(2):137–143.
40. Cedervall T, Lynch I, Lindman S, Berggård T, Thulin E, Nilsson H, Dawson KA, Linse S. Understanding the nanoparticle–protein corona using methods to quantify exchange rates and affinities of proteins for nanoparticles. Proc Natl Acad Sci USA. 2007; 104(7):2050–2055. [PubMed: 17267609]
41. Wei T, Liu J, Ma H, Cheng Q, Huang Y, Zhao J, Huo S, Xue X, Liang Z, Liang XJ. Functionalized Nanoscale Micelles Improve Drug Delivery for Cancer Therapy in Vitro and in Vivo. Nano Lett. 2013; 13(6):2528–2534. [PubMed: 23634882]
42. Liu J, Ma X, Jin S, Xue X, Zhang C, Wei T, Guo W, Liang XJ. Zinc Oxide Nanoparticles as Adjuvant To Facilitate Doxorubicin Intracellular Accumulation and Visualize pH-Responsive Release for Overcoming Drug Resistance. Mol Pharm. 2016; 13(5):1723–1730. [PubMed: 27070828]

43. Davis ME, Chen Z, Shin DM. Nanoparticle therapeutics: an emerging treatment modality for cancer. Nat Rev Drug Discov. 2008; 7(9):771–782. [PubMed: 18758474]
44. Nel AE, Madler L, Velegol D, Xia T, Hoek EMV, Somasundaran P, Klaessig F, Castranova V, Thompson M. Understanding biophysicochemical interactions at the nano-bio interface. Nat Mater. 2009; 8(7):543–557. [PubMed: 19525947]
45. Adler J, Parmryd I. Quantifying colocalization by correlation: The Pearson correlation coefficient is superior to the Mander's overlap coefficient. Cytometry Part A. 2010; 77A(8):733–742.
46. Barlow AL, MacLeod A, Noppen S, Sanderson J, Guérin CJ. Colocalization Analysis in Fluorescence Micrographs: Verification of a More Accurate Calculation of Pearson's Correlation Coefficient. Microsc Microanal. 2010; 16(6):710–724. [PubMed: 20946701]
47. Peiris PM, Abramowski A, McGinnity J, Doolittle E, Toy R, Gopalakrishnan R, Shah S, Bauer L, Ghaghada KB, Hoimes C, Brady-Kalnay SM, Basilion JP, Griswold MA, Karathanasis E. Treatment of Invasive Brain Tumors Using a Chain-like Nanoparticle. Cancer Res. 2015; 75(7): 1356–1365. [PubMed: 25627979]
48. Vassallo I, Zinn P, Lai M, Rajakannu P, Hamou MF, Hegi ME. WIF1 re-expression in glioblastoma inhibits migration through attenuation of non-canonical WNT signaling by downregulating the lncRNA MALAT1. Oncogene. 2015:12–21. [PubMed: 25772239]
49. Lu-Emerson C, Duda DG, Emblem KE, Taylor JW, Gerstner ER, Loeffler JS, Batchelor TT, Jain RK. Lessons From Anti-Vascular Endothelial Growth Factor and Anti-Vascular Endothelial Growth Factor Receptor Trials in Patients With Glioblastoma. J Clin Oncol. 2015; 33:1197–1213. [PubMed: 25713439]
50. Owens DE, Peppas NA. Opsonization, biodistribution, and pharmacokinetics of polymeric nanoparticles. Int J Pharm. 2006; 307(1):93–102. [PubMed: 16303268]
51. Moghimi SM, Szebeni J. Stealth liposomes and long circulating nanoparticles: critical issues in pharmacokinetics, opsonization and protein-binding properties. Prog Lipid Res. 2003; 42(6):463–478. [PubMed: 14559067]

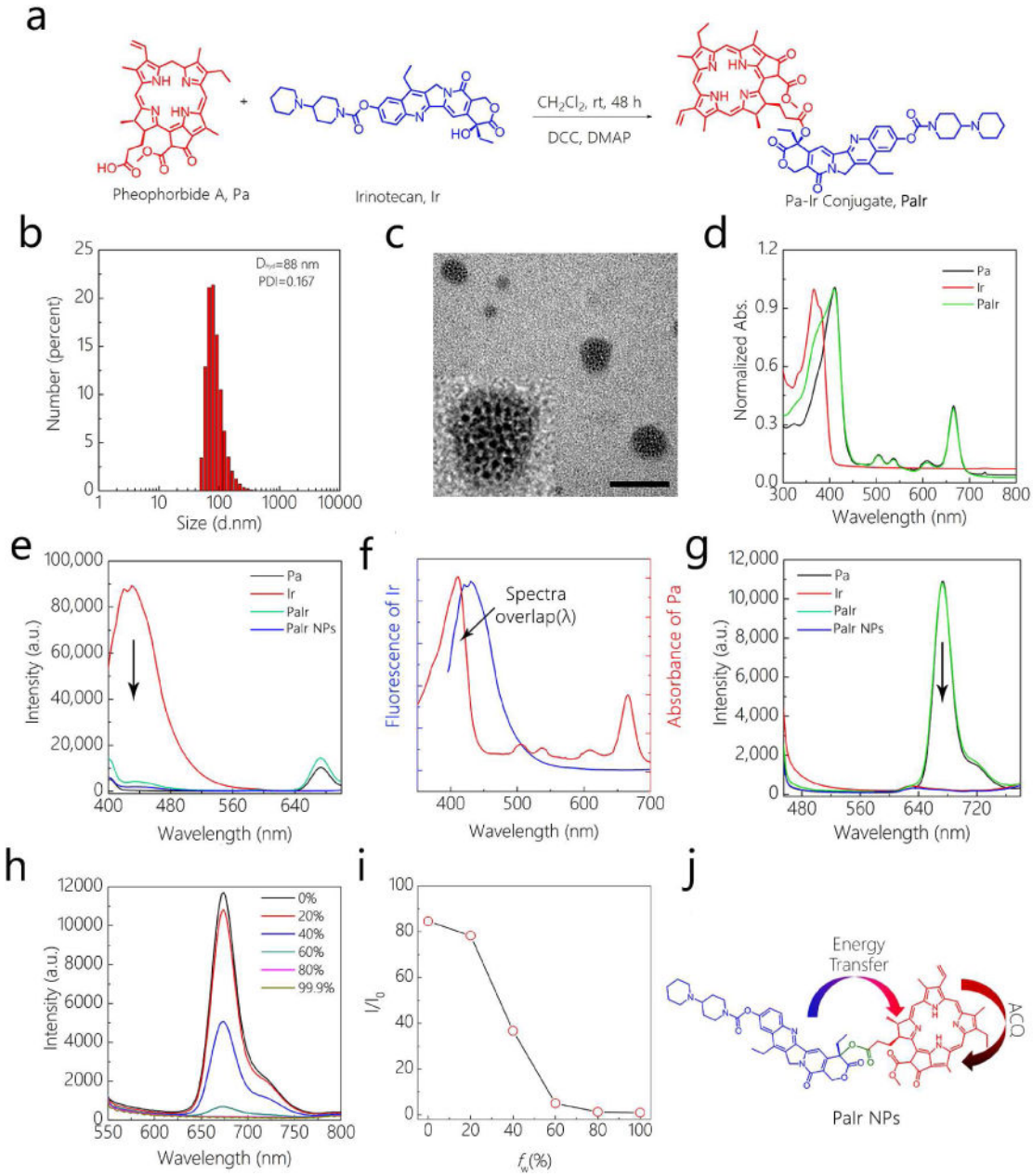

Figure 1.

a) Chemical synthesis of PaIr monomer; b) Size distributions and polydispersity index (PDI) of PaIr NPs; c) TEM micrograph of PaIr NPs; d) UV-Vis absorbance of Pa, Ir and PaIr; e) Fluorescence behaviors of Pa, Ir, PaIr and PaIr NPs. Excitation was 370 nm (the optimal excitation of Ir); f) Spectra overlap between emission of Ir and absorbance of Pa; g) Fluorescence spectra Pa, Ir, PaIr and PaIr NPs with excitations of 412 nm (the maximum absorbance of Pa); h) Fluorescence behaviors of Pa (in PaIr monomers) dissolved in different fractions of water, f_w (%) denotes a water content in DMSO (percentage in volume); i) Plot calculated from h) showing the ACQ behavior of Pa. j) Illustration of energy transfer relay in PaIr NPs. All materials were set to 50 μM.

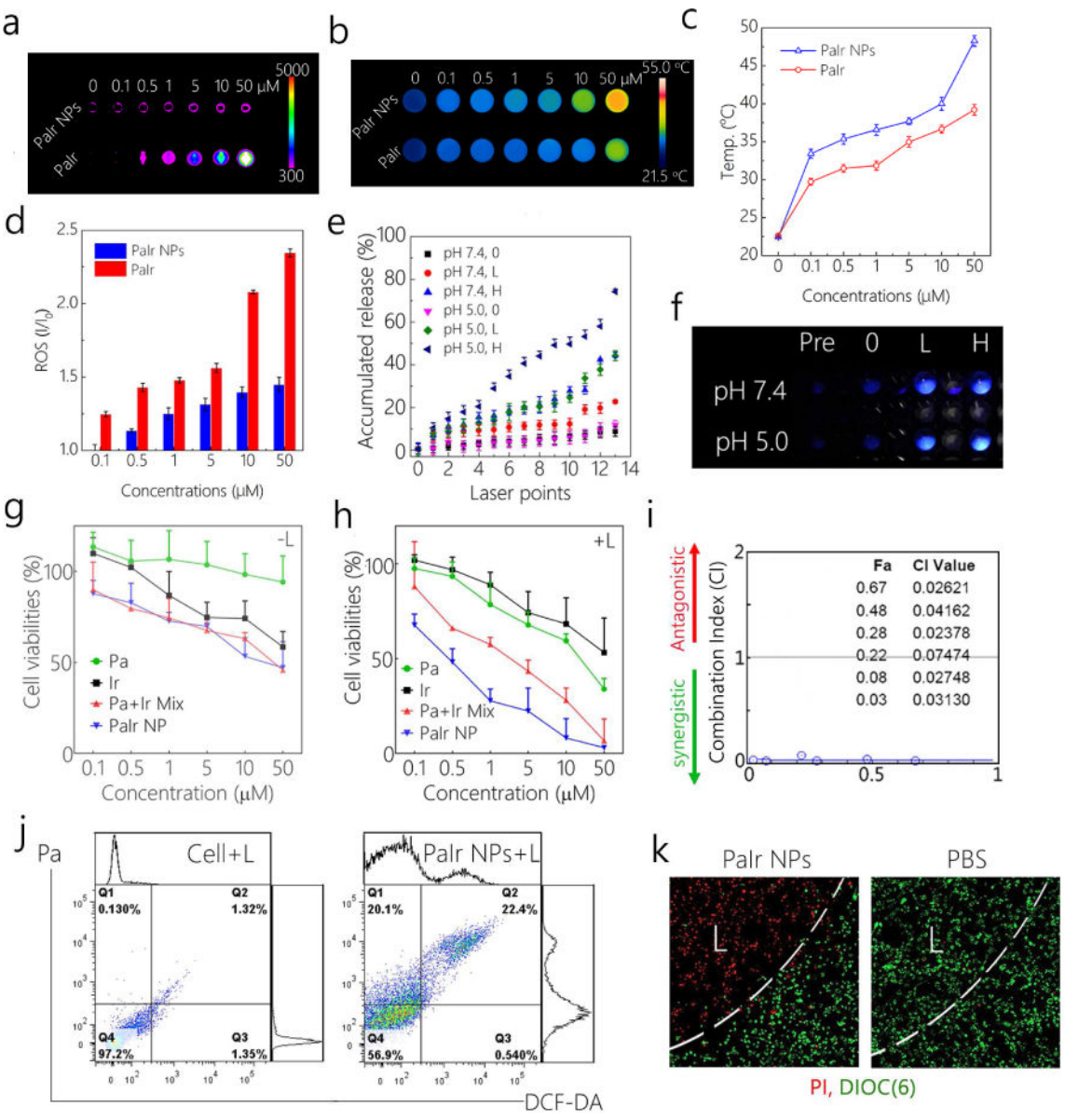

Figure 2.

a) NIRFI of PaIr monomer and PaIr NPs. b) Thermal images and c) Quantitative temperature variations of PaIr NPs and PaIr monomer. d) ROS generations of PaIr NPs. PaIr NPs were irradiated by NIR laser (680 nm) at 0.3 w/cm^2 for 3 min. e) Accumulated drug release of PaIr NPs in pH 7.4 and pH 5.0, with or without laser treatments. f) Blue fluorescence recovery of Ir indicated drug release of PaIr NPs. The image was captured under 365 nm UV lamp. “Pre” denoted the control samples before laser treatments (fresh made). “0” denoted non-laser treated samples, and “L” and “H” corresponded to low and high laser powers respectively. Cell viabilities of PaIr NPs towards U87-MG tumor cells g) without or h) with laser treatments. i) Combination index (CI) illustrated the synergistic effect of phototherapy and chemotherapy. CI versus Fraction affected (Fa) plot was calculated based on Figure 2h. j) FACS quantitatively exhibited the ROS production of PaIr NPs in U87-MG tumor cells.

The ROS production indicated by a ROS indicator, 2′,7′-dichlorofluorescin diacetate (DCF-DA), Pa denoted the fluorescence of PaIr NPs. k) Light-triggered controllable and precise cancer therapy in cellular level. 3,3′-Dihexyloxacarbocyanine Iodide, DIOC(6) indicates live cells (green), Propidium iodide (PI) stains dead cells (red). The laser treated areas were marked with ‘L’. The scale bar is 200 μm.

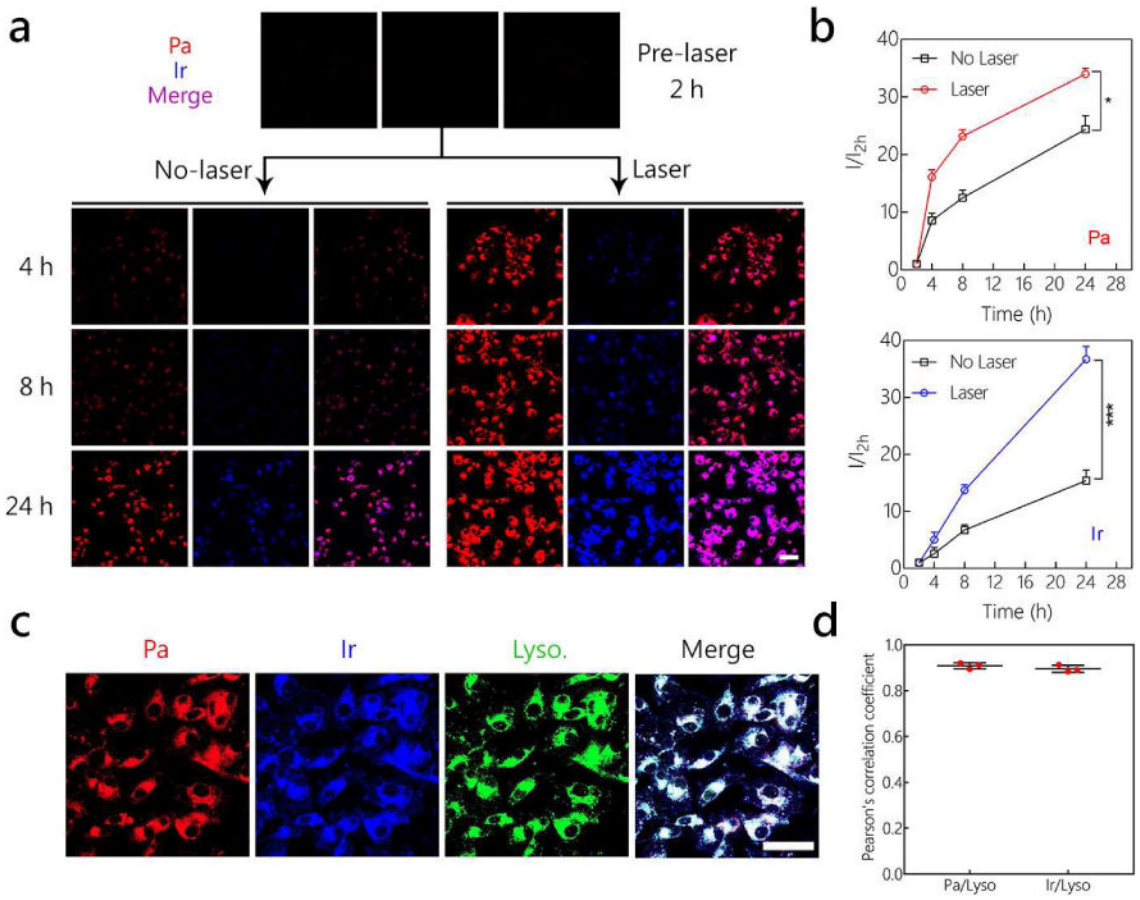

Figure 3.

a) Self-indication of cellular behaviors and time-dependent drug release of PaIr NPs (10 μM) by observing the dual-color fluorogenic process of Pa and Ir. The scale bar is 50 μm. b) Quantification of the dual-color fluorogenic process in a) by ImageJ. *p<0.05. ***p<0.001. c) Lysosomes colocalization of PaIr NPs in U87-MG cells. Cells were treated with the identical procedures of a), and stained with LysoTracker™ Green DND-26 for 30 min, then observed by CLSM. The scale bar is 50 μm. d) Quantification of the lysosomes colocalization. Pearson's correlation coefficient was employed to denote colocalization efficiency.

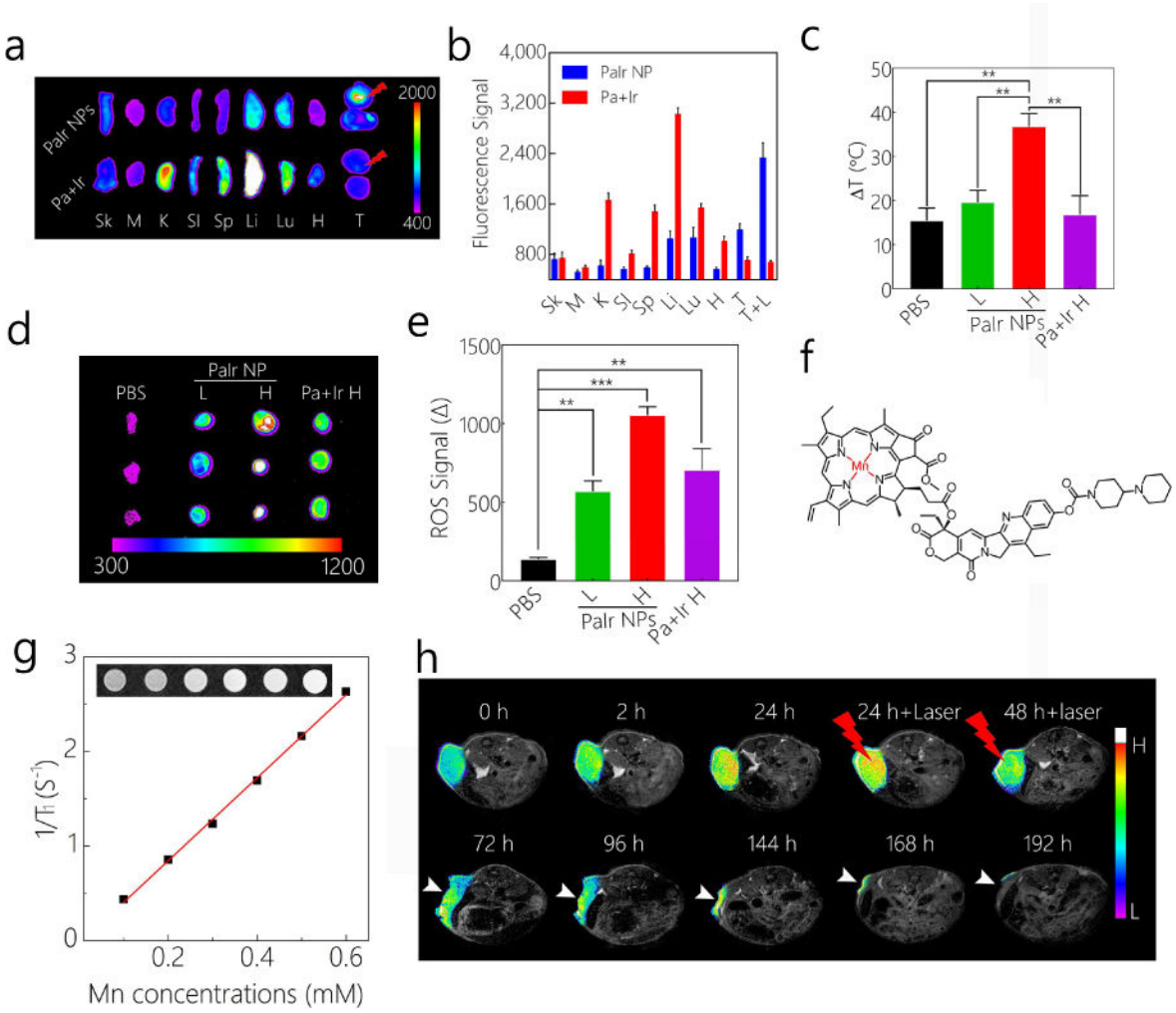

Figure 4.

a) *Ex vivo* distribution of PaIr NPs indicated by intrinsic NIRF, Pa+Ir mixture treated groups were set as control. To illustrate the effect of laser, mice were inoculated with two tumors on each flank, and one tumor was treated with laser. The upper tumor was treated with laser after 24 h administration of PaIr NPs. The mice (n=3) were sacrificed 24 h after the laser treatment. Sk, skin; M, muscle; K, kidney; SI, small intestine; S, spleen; Li, liver; Lu, lung, H, heart; T, tumor. b) Quantitative data of the organs distributions in a). c) Photothermal effects of PBS, PaIr NPs L, PaIr NPs H, and Pa+Ir H groups. Laser treatments were introduced 24 h after the materials administration, PBS group was treated with high laser dose. d) ROS production (Post-CellROX) and e) the statistics data on PBS, PaIr NPs L, PaIr NPs H and Pa+Ir H treated mice (n=3). ROS production was indicated by CellROX™ Deep Red Reagent. The ROS signal (Δ) was calculated by deducted NIRF signal of "pre-CellROX" from the "post-CellROX" readouts. **, $p<0.01$, ***, $p<0.001$. f) Chemical structure of Mn^{2+} chelated PaIr monomer. g) Concentration-dependent relaxation of Mn^{2+} chelated PaIr NPs. By calculation, the r^1 is 4.38 mM^{-1} S^{-1}. h) Self-indicated the phototherapeutic effect by T_1-weighted MRI. White arrows point the tumor. The light dose was 0.8 w/cm^2. Ir dose: 20 mg/kg, PaIr NPs dose: total 40 mg/kg (Pa 20 mg/kg & Ir 20 mg/

kg), and Pa+Ir dose: 20 mg/kg Pa mixed with 20 mg/kg Ir. High laser power was 0.8 w/cm^2, and low laser dose was 0.4 w/cm^2. All laser treatments lasted for 3 min.

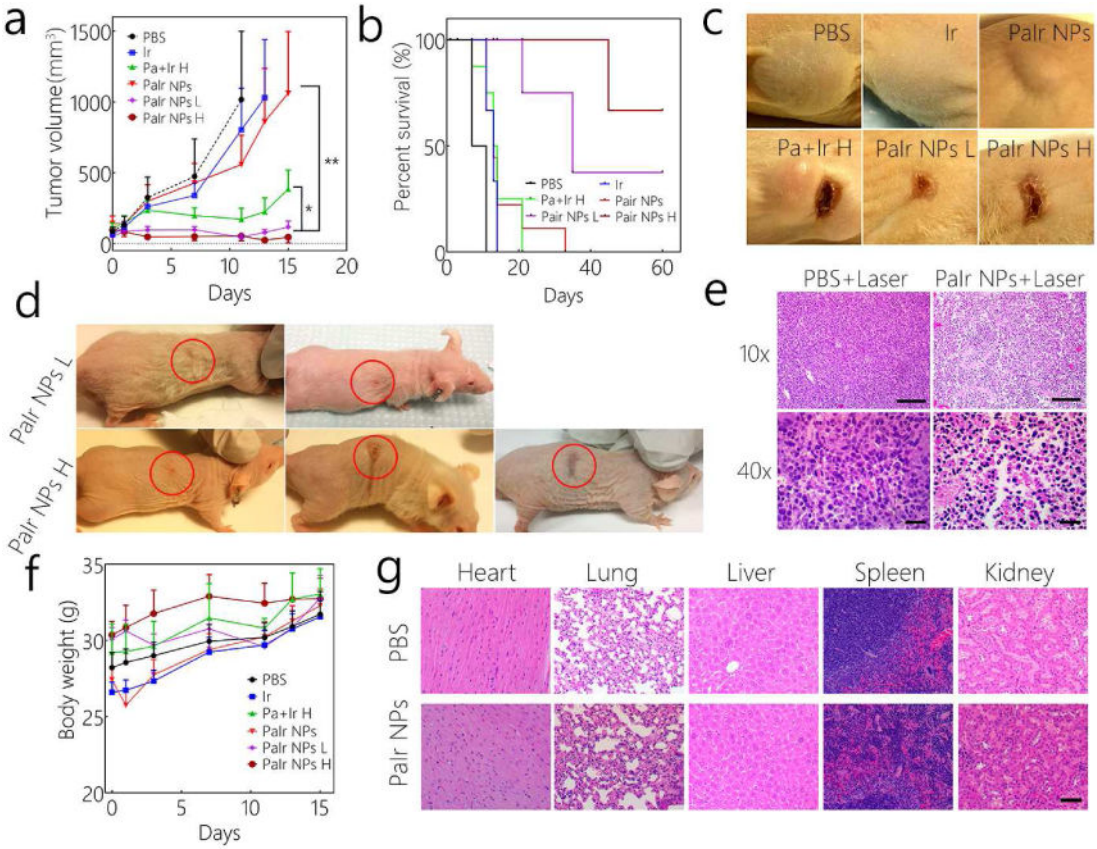

Figure 5.

a) Tumor volumes and b) Kaplan–Meier curves for PDX GBM bearing mice (n=6). c) Tumors images of each group after 2 doses treatments. d) The images of completely cured mice. The red circles denote the treated tumor region that after the laser burned scars naturally fell off. e) Histopathological evaluation of PBS or PaIr NPs treated tumors (with 0.8 w/cm^2 laser treatment). The scale bar in 10 × images is 200 μm, and in 40 × is 60 μm. f) Body weight changes of the PDX GBM-bearing mice (n=6). g) H&E staining of main organs of PaIr NPs treated mice, PBS-treated group was set as control. The scale bar was 100 μm. The light dose was 0.8 w/cm^2. Ir dose: 20 mg/kg, PaIr NPs dose: total 40 mg/kg (Pa 20 mg/kg & Ir 20 mg/kg), and Pa+Ir dose: 20 mg/kg Pa mixed with 20 mg/kg Ir. High laser power was 0.8 w/cm^2, and low laser dose was 0.4 w/cm^2. All laser treatments lasted for 3 min.

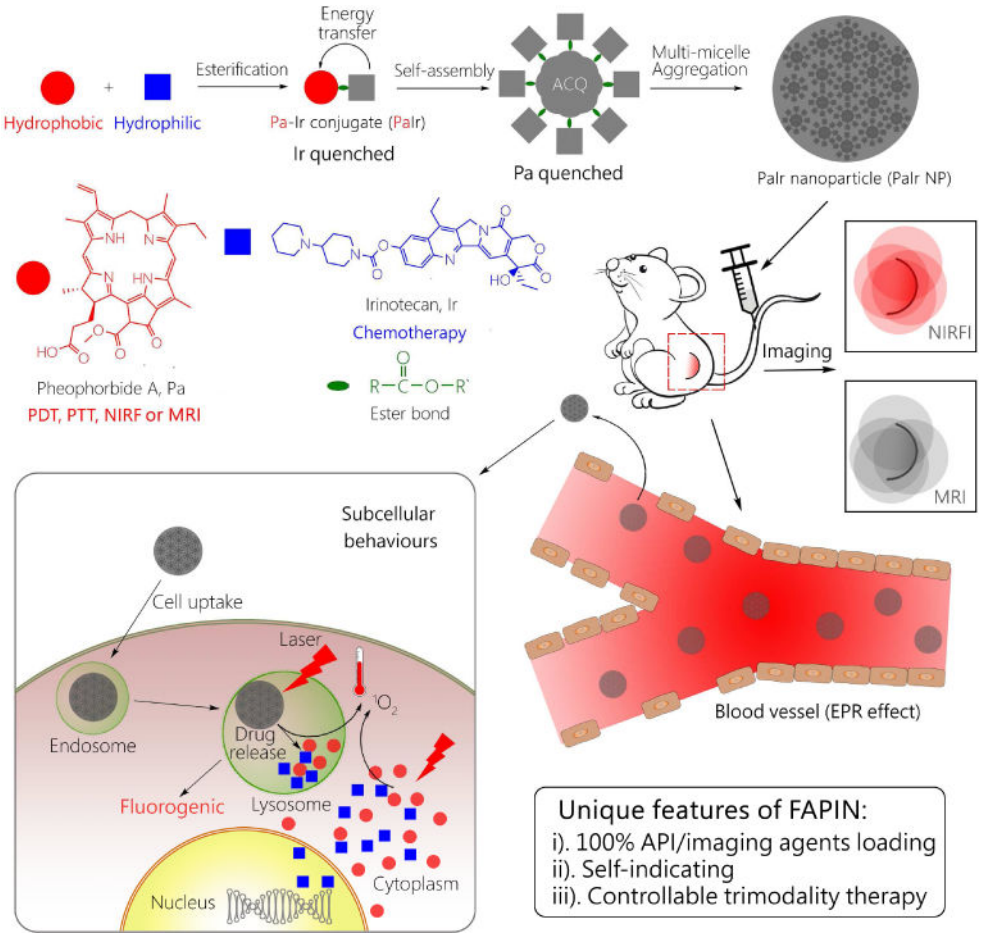

Scheme 1.

Schematic illustration of the self-indicating, fully active pharmaceutical ingredients nanoparticles (FAPIN).